Journal of Materials Chemistry A

Accepted Manuscript

ROYAL SOCIETY OF CHEMISTRY

www.rsc.org/materialsA

New $Cr_2Mo_3O_{12}$-based Anodes：Morphology Tuning and Li-Storage Properties

Lei Guo and Yong Wang*

Department of Chemical Engineering, School of Environmental and Chemical Engineering,Shanghai University, Shangda Road 99, Shanghai, P. R. China, 200444

Phone: +86-21-66137723. Fax: +86-21-66137725. Email: yongwang@shu.edu.cn

Abstract

A new ternary metal oxide ($Cr_2Mo_3O_{12}$) anode with its application as an anode material for Li-ion batteries is reported in this work. Experimental conditions such as reaction temperature, reaction time, and reactant concentration have all been investigated. The product can be obtained with sheet-like or rod-like morphology with/without the presence of graphene support. The $Cr_2Mo_3O_{12}$/graphene rod-on-sheet composite is found to be more suitable for Li-storage compared to the $Cr_2Mo_3O_{12}$/graphene sheet-on-sheet composite and pristine $Cr_2Mo_3O_{12}$ nanosheets/nanorods. The rod-on-sheet composite delivers a large reversible capacity of 988 mAh g^{-1} after 50 cycles at a current density of 100 mA g^{-1} and a good rate capability. Moreover, a preliminary Li-storage mechanism is also explored and suggested.

Keywords: $Cr_2Mo_3O_{12}$, nanorod, nanosheet, graphene, lithium ion batteries

Introduction

Rechargeable lithium-ion batteries (LIBs), as the most rapidly growing energy storage system, have been widely used in portable electronic devices, hybrid electrical vehicles, and electrical vehicles.[1-3] The current commercial LIBs gradually cannot meet the ever-growing demands for high energy and power density. In recent years, great efforts have been made to seek alternative electrode material which plays a vital role in improving the performance of LIBs.[4-5] Transition metal oxides can deliver higher gravimetric and volumetric capacities compared with commercial graphite. For example, a theoretical capacity of 1058 or 1116 mAh g^{-1} can be calculated for chromic oxide (Cr_2O_3)[6-11] or molybdenum oxide (MoO_3)[12-15]. However, almost all transitional metal oxides exhibit poor electrical conductivity and a large volume change during the conversion reactions with lithium, which may significantly affect the electrochemical properties of electrode materials such as cycling performance and rate-capability.[4, 16]

To solve these problems, considerable amounts of attempts have been made to develop nanoscale electrode materials and produce a hybrid matrix with carbon materials (such as graphene and carbon nanotube).[17-25] These hybrid composites could benefit from not only the large Li-storage capacity of transitional metal oxides, but also the improved electrical conductivity and structure stability of carbon materials. Recently, Ternary metal oxides are expected to have unique lithium storage properties distinct from binary oxides, which are induced by the combination of two different metals in one matrix.[26-36] Multiple species of ternary metal oxides can be accessible due to the diversity of metal elements and crystal

structure[37-40], while controlled synthetic method and complicated lithium storage mechanism still leave a huge challenge.

Herein, this work reports a new ternary metal oxide ($Cr_2Mo_3O_{12}$) for lithium ion storage. $Cr_2Mo_3O_{12}$ was prepared with nanorod and nanosheet morphologies. Graphene was further used to improve its electrochemical properties in the $Cr_2Mo_3O_{12}$/graphene composites. It is found that a large reversible capacity could be achieved for graphene supported $Cr_2Mo_3O_{12}$ nanorods with good cycling performances. A preliminary Li-storage mechanism was also explored for this new anode.

Materials synthesis: All chemicals were used as received without further purification. Graphene (GNS) were prepared by a modified Hummers method, followed by a thermal reduction as reported previously[22]. In a typical synthesis of $Cr_2Mo_3O_{12}$ nanorods on graphene composite: GNS (38.7 mg) were dissolved in deionized water (25 mL) and then sonicated for 1 h. Hexaammonium heptamolybdate (AHM, 0.1 g) tetrahydrate and Chromium chloride hexahydrate ($CrCl_3 \cdot 6H_2O$, 0.1 g) were then added into the suspension with constant magnetic stirring. After adjusting pH to 1 using 15 wt % HCl solution, the mixture was transferred into Teflon-lined stainless steel autoclave and heated up to 180 °C for 12 h. The as-prepared precipitate was rinsed with deionized water for several times, and finally dried at 80 ^oC in vacuum for further characterization. To explore the effect of synthesis conditions, the intermediate products were collected when the reaction time was 8, 24 h and the reaction temperature was 100 ^oC. Besides, various amounts of GNS were also used for preparation of

$Cr_2Mo_3O_{12}$/graphene rod-on-sheet composites with different contents of GNS to optimize lithium storage performance. $Cr_2Mo_3O_{12}$/graphene sheet-on-sheet composites were prepared in a similar method by adding 0.02 g instead of 0.1 g $CrCl_3 \cdot 6H_2O$. Rod-like $Cr_2Mo_3O_{12}$ and sheet-like $Cr_2Mo_3O_{12}$ product were prepared by a similar method in the absence of GNS, respectively.

Materials characterization: The samples were characterized by X-ray diffraction (XRD, Rigaku D/max-2550V, Cu Kα radiation), field-emission scanning electron microscopy (FE-SEM, JSM-6700F) with an energy dispersive X-ray spectrometer (EDS), transmission electron microscopy and high-resolution transmission electron microscopy (TEM, HRTEM, JEOL JEM-200CX and JEOL 2010F). Raman spectroscopy was recorded on Renishaw in plus laser Raman spectrometer (excitation wavelength: 785 nm, excitation power: 3 mW, spot size: ~1.2 μm). The Brunauer-Emmett-Teller (BET) surface area and porous structures were determined by an accelerated surface area and porosimetry analyzer (Micromeritics Instrument Corp, ASAP 2020 M + C, analysis adsorptive: N_2). The contents of carbon were measured using an elemental analyzer (Vario Micro).

Electrochemical measurements: The Swagelok-type cells were assembled in an argon-filled glove-box and used to measure the electrochemical performances. The working electrodes were composed of active material, acetylene black and poly (vinylidene difluoride) (PVDF) at a weight ratio of 80: 10: 10 in N-methyl pyrrolidinone (NMP). The loading amount of the electrode on copper foil was kept at ~2 mg cm^{-2} and the thickness was ~20 micrometers.

Lithium foil was used as the reference electrode. The electrolyte was 1 M $LiPF_6$ dissolved in a mixture of ethylene carbonate (EC) and diethyl carbonate (DEC) (1: 1 w/w). The galvanostatic discharged (lithium insertion) and charged (lithium extraction) tests were performed at various current densities (100-1000 mA g^{-1}) in the fixed voltage range 5 mV to 3.0 V. Cyclic voltammetry (CV) was performed on a CHI660D electrochemical workstation at a scan rate of 0.1 mV s^{-1}. Nyquist plots were collected on the same workstation for various electrodes from 100 kHz to 0.01 Hz.

Results and Discussion

Materials Synthesis and Characterizations:

For the synthesis of $Cr_2Mo_3O_{12}$ nanorods on graphene composite, a mixture solution with regulated pH value is introduced as the precursor, followed by a one-step hydrothermal method. The crystalline phases of the obtained products are firstly identified by XRD in Fig. 1a. The sharp peaks can be easily indexed to $Cr_2Mo_3O_{12}$, which are in good agreement with the standard data (PDF 20-0310). Similarly, the pristine $Cr_2Mo_3O_{12}$ nanorods without adding graphene are also obtained with highly crystalline structure. The morphology and structure of $Cr_2Mo_3O_{12}$-graphene composites are elucidated by SEM and TEM. The stretched lamellar structure of graphene is observed in Fig. 1b. Fig. 1c shows the TEM image of pristine $Cr_2Mo_3O_{12}$ rods with ~400 nm in length and ~30 nm in diameter. Fig. 1d-e show the graphene supported $Cr_2Mo_3O_{12}$ composite. A large number of $Cr_2Mo_3O_{12}$ rods are uniformly distributed and wrapped by graphene nanosheets. Compared with pristine $Cr_2Mo_3O_{12}$, the $Cr_2Mo_3O_{12}$ rods in the composite have no significant morphology change. The EDS spectrum

and elemental mapping images for $Cr_2Mo_3O_{12}$/graphene rod-on-sheet composites are shown in Fig. 1f and Fig. 2. A few elements such as Mo, Cr and C are observed and distributed uniformly in the composite, indicating the uniformly graphene-wrapped rod-like $Cr_2Mo_3O_{12}$ nanostructure. The atomic ratio of Cr to Mo is estimated to be ~1:1.6, which is approaching the theoretical value of 1:1.5.

The TEM and HRTEM measurements were carried out to provide in-depth information about the morphology and structure of the $Cr_2Mo_3O_{12}$/graphene rod-on-sheet composites. Fig. 3a-b show the TEM images at different magnifications. The $Cr_2Mo_3O_{12}$ rods with 200-500 nm in length and ~30 nm in diameter are distributed on the graphene nanosheets, which is in accordance with the SEM results. As shown in Fig. 3c, the lattice fringe of ~0.38 nm are observed, corresponding to the (103) plane of $Cr_2Mo_3O_{12}$. Fig. 3d shows the SAED pattern consisting of bright spots with (103), (122), (131) and (141) planes.

Fig. 4 shows different XRD patterns of the obtained products when temperature is performed at 100 ^oC and 180 ^oC for 12 h, respectively. The product appears to be largely amorphous at 100 ^oC. When the temperature is increased to 180 ^oC, several characteristic diffraction peaks of the product can be well indexed to $Cr_2Mo_3O_{12}$. It is indicated that the crystalline structure of the products is closely related to the reaction temperature. Fig. 5a shows XRD patterns of the obtained products prepared at 180 ^oC for 8, 12 and 24 h, respectively. Obviously, there is no significant change in the XRD patterns, which can all be indexed to $Cr_2Mo_3O_{12}$. Nevertheless, the distinct size change in terms of length and diameter can be observed for $Cr_2Mo_3O_{12}$ as indicated by TEM images in Fig. 5b-d. Most $Cr_2Mo_3O_{12}$ nanorods (8 h) are

observed with the length less than 200 nm and the diameter larger than 40 nm (Fig. 5b). When the reaction time is increased to 12 h (Fig. 5c) and 24 h (Fig. 5d), $Cr_2Mo_3O_{12}$ nanorods become longer in length and thinner in diameter. The product (24 h) exhibits a diameter less than 20 nm and a length around 1μm. It is indicated that the reaction time is another factor to affect the size and morphology of the product. Fig. 6a shows XRD patterns of the obtained $Cr_2Mo_3O_{12}$ nanosheets and $Cr_2Mo_3O_{12}$/graphene sheet-on-sheet products when a small amount (0.02 g) of $CrCl_3 \cdot 6H_2O$ is used in the hydrothermal reaction at 180 ^oC for 12 h. These diffraction peaks are very similar to $Cr_2Mo_3O_{12}$ nanorods and the $Cr_2Mo_3O_{12}$/graphene rod-on-sheet composite. Sheet-like $Cr_2Mo_3O_{12}$ structure (several micrometers in size) with a heavy agglomeration is observed in Fig. 6b. Fig. 6c shows SEM image of graphene sheets supported sheet-like $Cr_2Mo_3O_{12}$. Several elements such as Mo, Cr, O and C are observed in the EDS spectrum in Fig. 6d. As shown in the TEM image of Fig. 6e, the sheet-like $Cr_2Mo_3O_{12}$ with ~500 nm in size can be observed in the presence of graphene nanosheets. The thickness of $Cr_2Mo_3O_{12}$ nanosheet is estimated to be ~35 nm based on the inset cross-section TEM image in Fig. 6f. A clear lattice fringe with a planar spacing of ~0.43 nm is observed in Fig. 6g, which can be assigned to the (021) plane of $Cr_2Mo_3O_{12}$.

Fig. 7a displays Raman spectra of various $Cr_2Mo_3O_{12}$-based composites with characteristic D-band at ~1320 cm^{-1} and G-band at ~1590 cm^{-1}. The D/G intensity ratios of the $Cr_2Mo_3O_{12}$/graphene rod-on-sheet and $Cr_2Mo_3O_{12}$/graphene sheet-on-sheet composites are calculated to be 1.45 and 1.42, which are both larger than bare graphene (1.18), indicating an increase of disordered domains of graphene after hybridizing. By an elemental analyzer, the

graphene contents in the composites can be determined to be ~24.0% and 26.8% for the $Cr_2Mo_3O_{12}$/graphene rod-on-sheet and $Cr_2Mo_3O_{12}$/graphene sheet-on-sheet composites, respectively. Nitrogen adsorption-desorption isotherms of $Cr_2Mo_3O_{12}$-based composites are shown in Fig. 7b-c and their pore size distribution curves are shown in the corresponding inset images based on the data of adsorption branch. Specific surface areas (BET) of 139.9 and 84.7 m^2/g for the $Cr_2Mo_3O_{12}$/graphene rod-on-sheet and $Cr_2Mo_3O_{12}$/graphene sheet-on-sheet are evaluated based on the isotherms curves.

Electrochemical Properties:

Fig. 8a shows the cyclic voltammogram curve of the $Cr_2Mo_3O_{12}$/graphene rod-on-sheet electrode. There are two cathodic peaks at ~1.84 and 1.54 V, corresponding to the stepwise lithium insertion into the electrode. A broad peak (~0.8 V) can be attributed to the decomposition of electrolyte and the formation of the solid electrolyte interface (SEI) film on graphene surface. In the anodic scan, a strong and broad peak at ~1.45 V can be ascribed to the reversible oxidation reaction of Cr and Mo elements. The low-density peak at ~2.37 V may be ascribed to the lithium extraction from Li_2MoO_4. Fig. 8b shows the first-cycle galvanostatic discharge (lithium insertion) and charge (lithium extraction) curves of graphene, sheet-like $Cr_2Mo_3O_{12}$, rod-like $Cr_2Mo_3O_{12}$, the $Cr_2Mo_3O_{12}$/graphene sheet-on-sheet and $Cr_2Mo_3O_{12}$/graphene rod-on-sheet composites at a current density of 100 mA g^{-1}. Initial discharge and charge capacities of $Cr_2Mo_3O_{12}$/graphene sheet-on-sheet electrode are evaluated to be 1920 and 1140 mAh g^{-1}. In comparison, the $Cr_2Mo_3O_{12}$/graphene rod-on-sheet composite exhibits slightly larger discharge and charge capacities of 1971 mAh

g^{-1} and 1221 mAh g^{-1}. It is worth noting that the first-cycle reversible charge capacities of two composites are both larger than pristine sheet-like $Cr_2Mo_3O_{12}$ (931 mAh g^{-1}) or rod-like $Cr_2Mo_3O_{12}$ (945 mAh g^{-1}).

Fig. 8c shows the cycling performances of various products at a current density of 100 mA g^{-1}. Compared with a small reversible capacity of 482 mAh g^{-1} for rod-like $Cr_2Mo_3O_{12}$ and 296 mAh g^{-1} for graphene after 50 cycles, the $Cr_2Mo_3O_{12}$/graphene rod-on-sheet composite exhibits more stable cycling performances. A large reversible capacity of 988 mAh g^{-1} could be still retained after 50 cycles. This may be ascribed to the synergetic effect between graphene and $Cr_2Mo_3O_{12}$. First, the drastic volume change of $Cr_2Mo_3O_{12}$ during cycling can be buffered and the restacking of graphene can be prevented effectively in the composite. Second, the unique one dimension structure of rod-like $Cr_2Mo_3O_{12}$ product and a large surface area of graphene nanosheets could help shorten the diffusion distance for mass and charge transport.[16-19] In comparison, the $Cr_2Mo_3O_{12}$/graphene sheet-on-sheet composite has a capacity fading from 1140 mAh g^{-1} to 721 mAh g^{-1} after 50 cycles. A small reversible capacity of 243 mAh g^{-1} is observed for pristine sheet-like $Cr_2Mo_3O_{12}$. The worse electrochemical properties of the sheet-like products compared to the corresponding rod-like products may be ascribed to the fact that $Cr_2Mo_3O_{12}$ sheets are quite thick based on the observations of SEM images (Fig. 6b-c and Fig. 6e-f). A smaller BET surface area is also observed for the sheet-on-sheet composite compared to the rod-on-sheet composite.

Moreover, Fig. 8d shows rate performances of various products at various current densities of

100, 500 and 1000 mA g^{-1}. When the current density is increased to 500 mA g^{-1}, a charge capacity of 786 mAh g^{-1} can be observed after cycling. Even at a high current density of 1000 mA g^{-1}, the charge capacity is still as high as 577 mAh g^{-1}. When the density comes back to a low current density of 100 mA g^{-1}, the $Cr_2Mo_3O_{12}$/graphene rod-on-sheet still maintains excellent cycling stability and a high charge capacity of 1009 mAh g^{-1} can be retained after 50 cycles. In comparison, the $Cr_2Mo_3O_{12}$/graphene sheet-on-sheet composite exhibits slightly lower reversible capacities. Reversible capacities of 611 and 452 mAh g^{-1} are observed at 500, 1000 mA g^{-1}, respectively. When the current density is changed back to 100 mA g^{-1}, the reversible capacity is 758 mAh g^{-1} after 50 cycles.

The electrochemical impedance spectra of sheet-like $Cr_2Mo_3O_{12}$, rod-like $Cr_2Mo_3O_{12}$, the $Cr_2Mo_3O_{12}$/graphene sheet-on-sheet, and $Cr_2Mo_3O_{12}$/graphene rod-on-sheet composites are shown in Fig. 9. The charge-transfer resistance (R_{ct}) of pristine $Cr_2Mo_3O_{12}$ nanosheet is determined to be 99 Ω based on the equivalent circuit, which is greatly reduced to 68.5 Ω in the sheet-on-sheet composite. The $Cr_2Mo_3O_{12}$/graphene rod-on-sheet composite also exhibits a much lower resistance of 28.7 Ω than the pristine rod-like $Cr_2Mo_3O_{12}$ (90 Ω). In general, the R_{ct} values of $Cr_2Mo_3O_{12}$/graphene composites are much smaller than those of pristine $Cr_2Mo_3O_{12}$ due to the presence of highly-conductive graphene. As a consequence, lithium diffusion and charge transfer should be facilitated for the graphene supported electrodes, which usually result in larger capacity and better high-rate performances.

To optimize the cycling performance for the $Cr_2Mo_3O_{12}$/graphene rod-on-sheet composite,

the effect of weight ratios of $Cr_2Mo_3O_{12}$ to graphene are investigated in Fig. 10. The galvanostatic charge-discharge characteristics of $Cr_2Mo_3O_{12}$/graphene rod-on-sheet composites with different graphene contents are shown in the Fig. 10a. The initial charge/discharge capacities are 1014/1648 and 1008/1619 mAh g^{-1} for $Cr_2Mo_3O_{12}$/graphene rod-on-sheet composites with 19.4 % and 30.9 % graphene respectively (the graphene contents were determined by an elemental analyzer). After 50 cycles, the MoO_2/graphene rod-on-sheet composites with 19.4 % and 30.9 % graphene show reversible capacities of 507 and 626 mAh g^{-1} in Fig. 10b. It can be indicated that the $Cr_2Mo_3O_{12}$/graphene rod-on-sheet composite with 24 % graphene content is close to the appropriate value of graphene content in the composite. A smaller amount of graphene in the composites may lead to the fact that the volume change of metal oxides cannot be buffered efficiently by graphene. On the other hand, a larger amount of graphene (a smaller amount of $Cr_2Mo_3O_{12}$) may cause the heavy re-stacking of graphene layers, thus losing graphene's intriguing properties[24,41].

The XRD tests of the discharged/charged electrodes to selected voltages were performed to explore its Li-storage mechanism in Fig. 11. A broad peak (centered at ~25°) can be observed for the electrode at various cycling stages, which is due to the presence of the conductive agent of carbon black. Obviously, two low-density peaks corresponding to Cr appear when the electrode is discharged to 1.5 V. When discharged to 1.0 V, the electrode exhibits another small peak appears at ~21°, which can be identified to be Li_2MoO_4. After a full discharge, no any crystalline peaks except for the broad peak for carbon black can be observed. It is indicated that the crystalline electrode has been transformed to amorphous phase after the

first full discharge. The electrode maintains amorphous structure when charged to 2 V. After the first full charge, a peak of MoO_3 appears, indicating the conversion storage mechanism of the Mo element. The SAED patterns of the electrodes were also obtained to investigate the phase change during cycling. The SAED pattern in Fig. 12a comprises several diffraction rings indicating the polycrystalline structure. The electrode becomes almost amorphous after the first discharge (Fig. 12b). After first full charge, several bright spots with diffuse set of rings appear and can be shown in Fig. 12c. The calculated planar spacing of 0.34 and 0.27 nm can be assigned to the (002) and (110) planes of MoO_3 (PDF 47-1320). These SAED results agree well with the observations of XRD patterns. Although there is no obvious evidence of the Cr_2O_3 phase (possibly amorphous) after the full charge, it is suggested that the ternary metal oxides ($Cr_2Mo_3O_{12}$) largely follow the conversion Li-storage mechanism of molybdenum oxide and chromic oxide. This is because if Cr element is not active, the large capacity approaching the theoretical capacities of two metal oxides cannot be achieved for the $Cr_2Mo_3O_{12}$ electrode. Moreover, there is a large lithium-insertion capacity occurred below 0.3 V for pristine $Cr_2Mo_3O_{12}$ nanosheet or nanorod electrode (Fig. 8b). Because the lithium insertion into Mo-based electrode usually takes place at higher voltages, the Cr element should be involved in the Li-storage reactions of the $Cr_2Mo_3O_{12}$ electrode.

Conclusion

In summary, unprecedented $Cr_2Mo_3O_{12}$-based anode materials were explored in this work. Sheet-like and rod-like $Cr_2Mo_3O_{12}$ products were successfully prepared with and without graphene support by adjusting experimental conditions. Electrochemical measurements

revealed that this ternary metal oxide may be a promising anode alternative because the $Cr_2Mo_3O_{12}$/graphene rod-on-sheet composite can exhibit a large reversible capacity of 988 mAh g^{-1} after 50 cycles. A preliminary Li-ion storage mechanism was also explored. Although the cycling performance is not very satisfactory, this work may pave the way for this new type of $Cr_2Mo_3O_{12}$ materials as a high-capacity anode candidate for lithium ion batteries.

Acknowledgements

The authors gratefully acknowledge the follow-up Program for Professor of Special Appointment in Shanghai (Eastern Scholar), the National Natural Science Foundation of China (51271105), Shanghai Municipal Government (11SG38,) and Innovative Research Team (IRT13078) for financial support. The authors also thank Lab for Microstructure, Instrumental Analysis and Research Center, Shanghai University, for materials characterizations.

References

[1] M. Armand and J. M. Tarascon, *Nature* 2008, **451**, 652-657.

[2] V. Etacheri, R. Marom, R. Elazari, G. Salitra and D. Aurbach, *Energy Environ. Sci.* 2011, **4**, 3243-3262.

[3] B. Scrosati and J. Garche, *J. Power Sources* 2010, **195**, 2419-2430.

[4] P. Poizot, S. Laruelle, S. Grugeon, L. Dupont and J. M. Tarascon, *Nature* 2000, **407**, 496-499.

[5] C. M. Park, J. H. Kim, H. Kim and H. J. Sohn, *Chem. Soc. Rev.* 2010, **39**, 3115-3141.

[6] W. B. Yue, S. S. Tao, J. M. Fu, Z. Q. Gao and Y. Ren, *Carbon* 2013, **65**, 97-104.

[7] Z. Q. Cao, M. L. Qin, B. R. Jia, L. Zhang, Q. Wan, M. S. Wang, A. A. Volinsky and X. H. Qu, *Electrochim. Acta* 2014, **139**, 76-81.

[8] H. Liu, X. W. Du, X. R. Xing, G. X. Wang and S. Z. Qiao, *Chem. Commun.* 2012, **48**, 865-867.

[9] B. K. Guo, M. F. Chi, X. G. Sun and S. Dai, *J. Power Sources* 2012, **205**, 495-499.

[10] F. Wang, W. Li, M. Y. Hou, C. Li, Y. G. Wang and Y. Y. Xia, *J. Mater. Chem. A* 2015, **3**, 1703-1708.

[11] G. X. Zhao, T. Wen, J. Zhang, J. X. Li, H. L. Dong, X. K. Wang, Y. G. Guo and W. P. Hu, *J. Mater. Chem. A* 2014, **2**, 944-948.

[12] Y. X. Sun, J. Wang, B. Zhao, R. Cai, R. Ran and Z. P. Shao, *J. Mater. Chem. A* 2013, **1**, 4736-4746.

[13] G. Y. Zhao, N. Q. Zhang and K. N. Sun, *J. Mater. Chem. A* 2013, **1**, 221-224.

[14] L. Q. Mai, B. Hu, W. Chen, Y. Y. Qi, C. S. Lao, R. S. Yang, Y. Dai and Z. L. Wang, *Adv. Mater.* 2007, **19**, 3712-3716.

[15] Z. Y. Wang, S. Madhavi and X. W. Lou, *J. Phys. Chem. C* 2012, **116**, 12508-12513.

[16] J. Jiang, Y. Y. Li, J. P. Liu, X. T. Huang, C. Z. Yuan and X. W. Lou, *Adv. Mater.* 2012, **24**, 5166-5180.

[17] K. T. Lee and J. Cho, *Nano Today* 2011, **6**, 28-41.

[18] Z. S. Wu, G. M. Zhou, L. C. Yin, W. C. Ren, F. Li and H. M. Cheng, *Nano Energy* 2012, **1**, 107-131.

[19] Y. Q. Sun, Q. Wu and G. Q. Shi, *Energy Environ. Sci.* 2011, **4**, 1113-1132.

[20] P. Chen, F. D. Wu and Y. Wang, *ChemSusChem* 2014, **7**, 1407-1414.

[21] Y. Gu, F. D. Wu and Y. Wang, *Adv. Funct. Mater.* 2013, **23**, 893-899.

[22] J. Kan and Y. Wang, *Sci. Rep.* 2013, **3**, 3502.

[23] Y. Gu, Y. Xu and Y. Wang, *ACS Appl. Mater. Interfaces* 2013, **5**, 801-806.

[24] L. Guo and Y. Wang, *Journal of Materials Chemistry A* 2015, **3**, 4706-715.

[25] P. Chen, Y. Su, H. Liu and Y. Wang, *ACS Appl. Mater. Interfaces* 2013, **5**, 12073-12082.

[26] B. Das, M. V. Reddy, C. Krishnamoorthi, S. Tripathy, R. Mahendiran, G. V. Subba Rao and B. V. R. Chowdari, *Electrochim. Acta* 2009, **54**, 3360-3373.

[27] N. N. Leyzerovich, K. G. Bramnik, T. Buhrmester, H. Ehrenberg and H. Fuess, *J. Power Sources* 2004, **127**, 76-84.

[28] Y. Ding, Y. Wan, Y. L. Min, W. Zhang and S. H. Yu, *Inorg. Chem.* 2008, **47**, 7813-7823.

[29] S. Komaba, N. Kumagai, R. Kumagai, N. Kumagai and H. Yashiro, *Solid State Ionics* 2002, **152-153**, 319-326.

[30] B. Das, M. V. Reddy, G. V. Subba Rao and B. V. R. Chowdari, *J. Solid State Electrochem.* 2008, **12**, 953-959.

[31] W. Xiao, J. S. Chen, C. M. Li, R. Xu and X. W. Lou, *Chem. Mater.* 2010, **22**, 746-754.

[32] S. S. Kim, S. Ogura, H. Ikuta, Y. Uchimoto and M. Wakihara, *Solid State Ionics* 2002, **146**, 249-256.

[33] Y. M. Sun, X. L. Hu, W. Luo and Y. H. Huang, *J. Mater. Chem.* 2011, **21**, 17229-17235.

[34] C. T. Cherian, M. V. Reddy, S. C. Haur and B. V. R. Chowdari, *ACS Appl. Mater. Interfaces* 2013, **5**, 918-923.

[35] Y. M. Sun, X. L. Hu, W. Luo, J. Shu and Y. H. Huang, *J. Mater. Chem. A* 2013, **1**, 4468-4474.

[36] Y. G. Liang, X. Y. Han, Z. H. Yi, W. C. Tang, L. Q. Zhou, J. T. Sun, S. J. Yang and Y. H. Zhou, *J. Solid State Electrochem.* 2007, **11**, 1127-1131.

[37] W. Li, Y. X. Yin, S. Xin, W. G. Song and Y. G. Guo, *Energy Environ. Sci.* 2012, **5**, 8007-8013

[38] Y. Wang and G. Z. Cao, *J. Mater. Chem.* 2007, **17**, 894-899.

[39] H. W. Shim, I. S. Cho, K. S. Hong, A. H. Lim and D. W. Kim, *J. Phys. Chem. C* 2011, **115**, 16228-16233.

[40] Y. Sharma, N. Sharma, G. V. Subba Rao and B. V. R. Chowdari, *Adv. Funct. Mater.* 2007, **17**, 2855-2861.

[41] W. W. Sun and Y. Wang, *Nanoscale* 2014, **6**, 11528-11552.

Figure Captions

Fig. 1 (a) XRD patterns of (i) the $Cr_2Mo_3O_{12}$/graphene rod-on-sheet composite and (ii) $Cr_2Mo_3O_{12}$ nanorods, (b) SEM image of graphene, (c) TEM image of $Cr_2Mo_3O_{12}$ nanorods, (d-e) SEM images of the $Cr_2Mo_3O_{12}$/graphene rod-on-sheet composite at low and high magnifications, (f) the EDS spectrum of the $Cr_2Mo_3O_{12}$/graphene rod-on-sheet composite.

Fig. 2 Elemental mapping images of the $Cr_2Mo_3O_{12}$/graphene rod-on-sheet composite. C, Cr, and Mo elements are distributed uniformly in the composite.

Fig. 3 The $Cr_2Mo_3O_{12}$/graphene rod-on-sheet composite: (a-b) TEM images at different magnifications, (c) HRTEM image, and (d) SAED pattern.

Fig. 4 XRD patterns of the $Cr_2Mo_3O_{12}$/graphene rod-on-sheet composites prepared at 100 ^oC and 180 ^oC for 12 h.

Fig. 5 (a) XRD patterns of the $Cr_2Mo_3O_{12}$/graphene rod-on-sheet composite prepared at 180 ^oC for 8, 12, and 24 h. TEM images of the $Cr_2Mo_3O_{12}$/graphene rod-on-sheet composites at 180 ^oC: (b) 8 h, (c) 12 h, (d) 24 h.

Fig. 6 (a) XRD patterns of (i) the $Cr_2Mo_3O_{12}$/graphene sheet-on-sheet composite (ii) $Cr_2Mo_3O_{12}$ nanosheets, (b) SEM image of $Cr_2Mo_3O_{12}$ nanosheets, the $Cr_2Mo_3O_{12}$/graphene sheet-on-sheet composite: (c) SEM image, (d) the EDS spectrum, (e) TEM image, (f) the inset image showing the cross-section, and (g) HRTEM image.

Fig. 7 (a) Raman spectra of various products, Nitrogen adsorption-desorption isotherms: (b) the $Cr_2Mo_3O_{12}$-graphene rod-on-sheet composite, (c) the $Cr_2Mo_3O_{12}$-graphene sheet-on-sheet composite.

Fig. 8 Electrochemical performances of various $Cr_2Mo_3O_{12}$ based anodes: (a) cyclic voltammograms, (b) the first-cycle discharge (lithium insertion) and charge (lithium extraction) curves, (c) cycling performance at a current density of 100 mA g^{-1} (0.1 C), (d) rate performances at various current densities of 100, 500 and 1000 mA g^{-1}.

Fig. 9 Nyquist plots of various $Cr_2Mo_3O_{12}$ based anodes.

Fig. 10 Electrochemical performances of the $Cr_2Mo_3O_{12}$/graphene rod-on-sheet composites with 19.4 %, 24 % and 30.9 % graphene: (a) the first-cycle discharge (lithium insertion) and charge (lithium extraction) curves, (b) cycling performance at a current density of 100 mA g^{-1} (0.1 C).

Fig. 11 XRD patterns of the electrodes obtained at different cycling stages.

Fig. 12 SAED patterns of the electrodes obtained at different cycling stages: (a) before cycling, (b) after first discharge, and (c) after first charge.

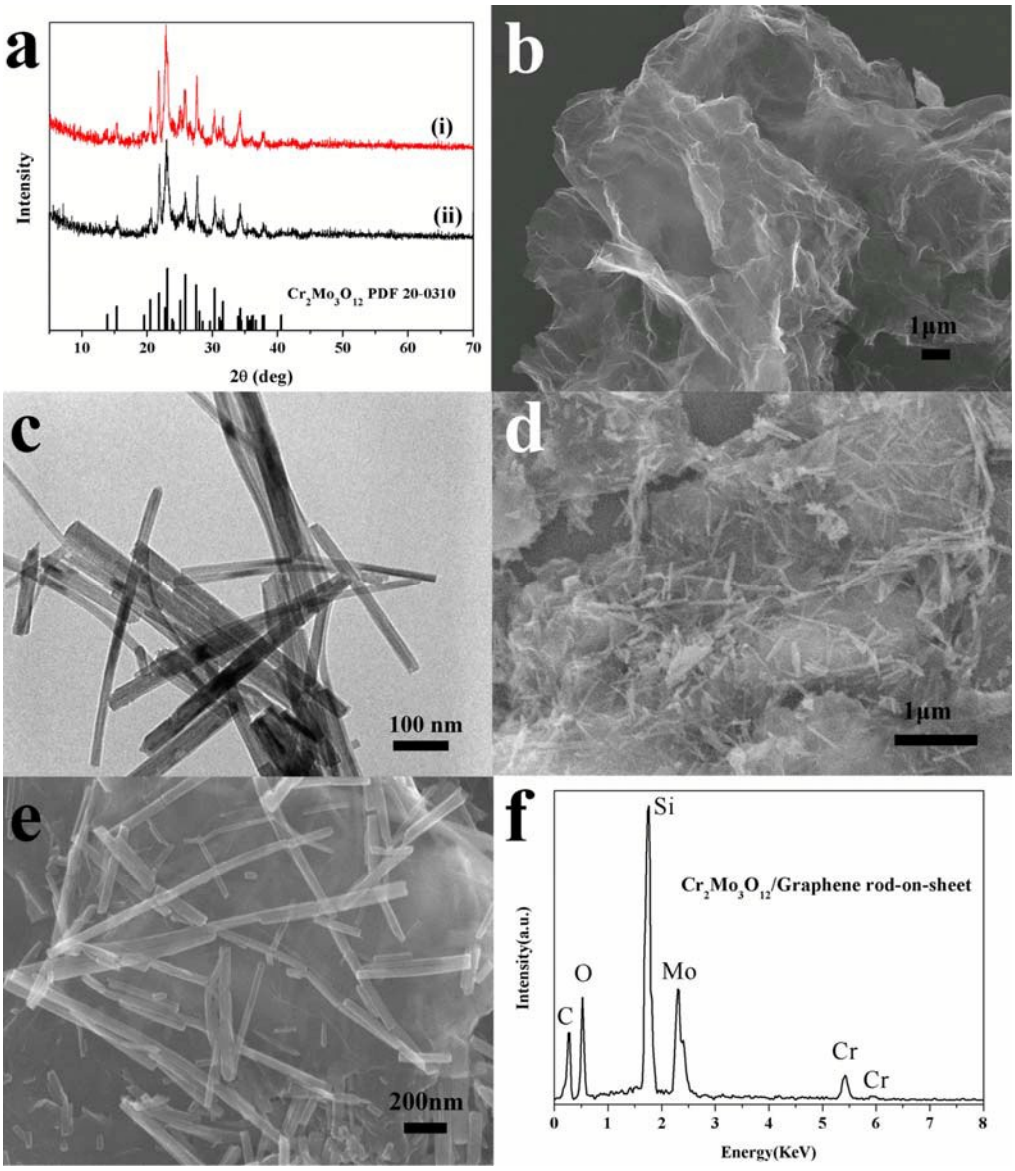

Fig. 1 (a) XRD patterns of (i) the $Cr_2Mo_3O_{12}$/graphene rod-on-sheet composite and (ii) $Cr_2Mo_3O_{12}$ nanorods, (b) SEM image of graphene, (c) TEM image of $Cr_2Mo_3O_{12}$ nanorods, (d-e) SEM images of the $Cr_2Mo_3O_{12}$/graphene rod-on-sheet composite at low and high magnifications, (f) the EDS spectrum of the $Cr_2Mo_3O_{12}$/graphene rod-on-sheet composite.

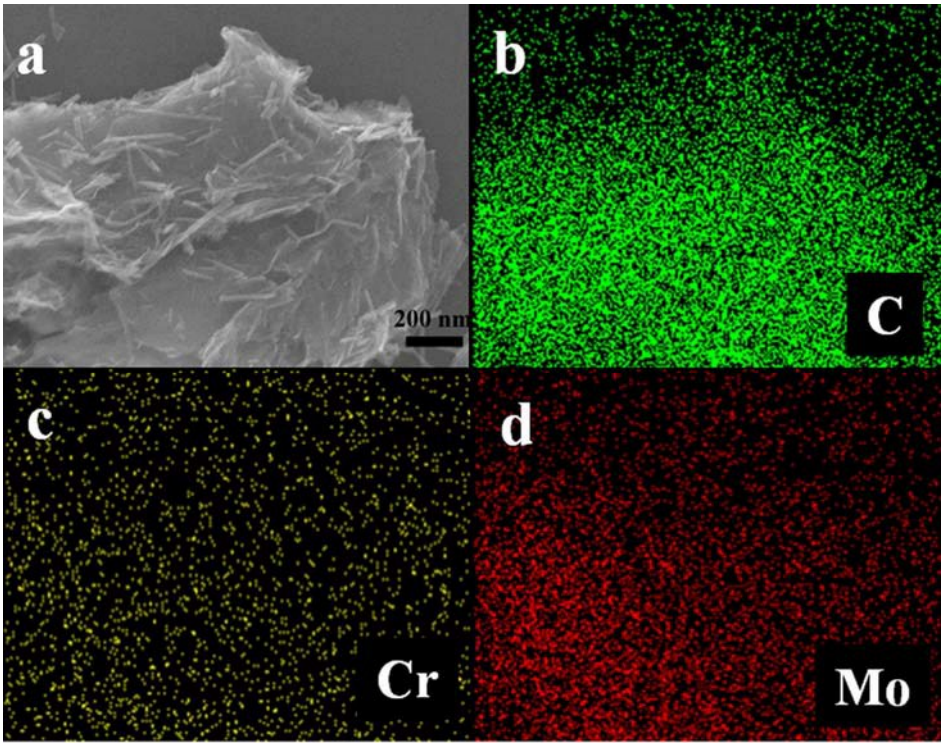

Fig. 2 Elemental mapping images of the $Cr_2Mo_3O_{12}$/graphene rod-on-sheet composite. C, Cr, and Mo elements are distributed uniformly in the composite.

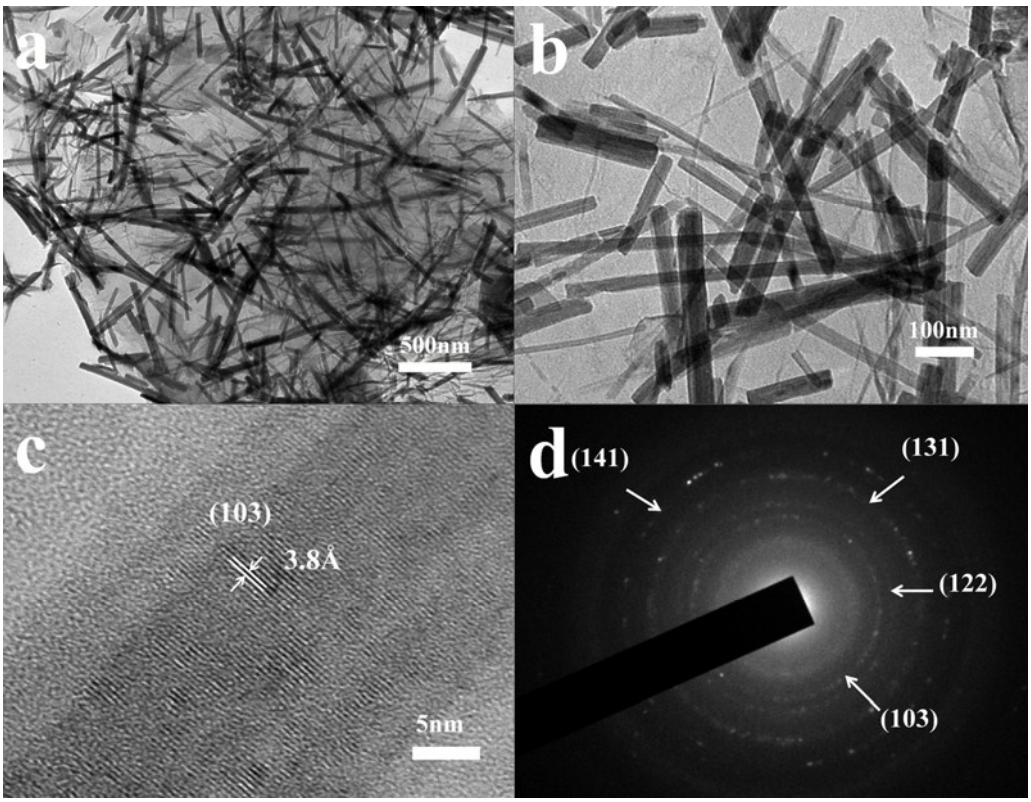

Fig. 3 The $Cr_2Mo_3O_{12}$/graphene rod-on-sheet composite: (a-b) TEM images at different magnifications, (c) HRTEM image, and (d) SAED pattern.

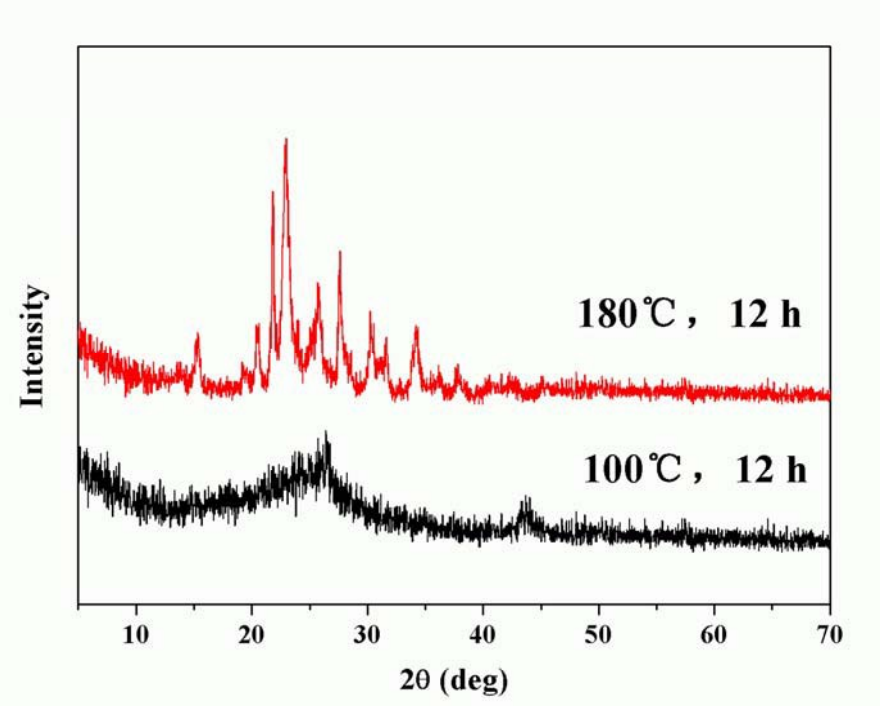

Fig. 4 XRD patterns of the $Cr_2Mo_3O_{12}$/graphene rod-on-sheet composites prepared at 100 ^oC and 180 ^oC for 12 h.

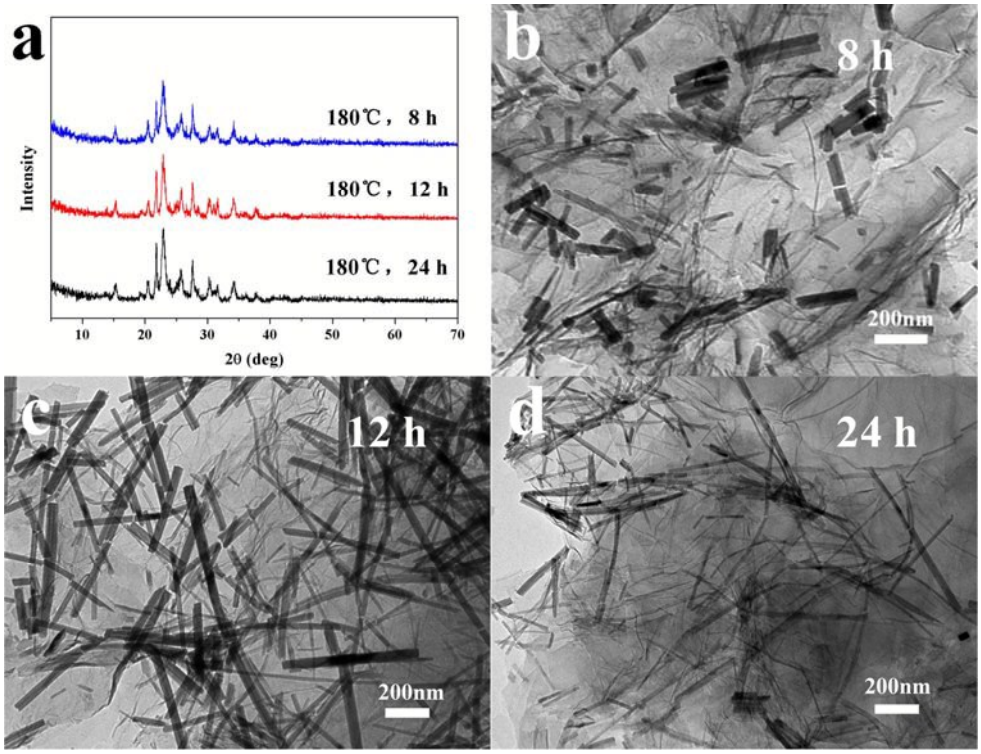

Fig. 5 (a) XRD patterns of the $Cr_2Mo_3O_{12}$/graphene rod-on-sheet composites prepared at 180 ^oC for 8, 12, and 24 h. TEM images of the $Cr_2Mo_3O_{12}$/graphene rod-on-sheet composites at 180 ^oC: (b) 8 h, (c) 12 h, (d) 24 h.

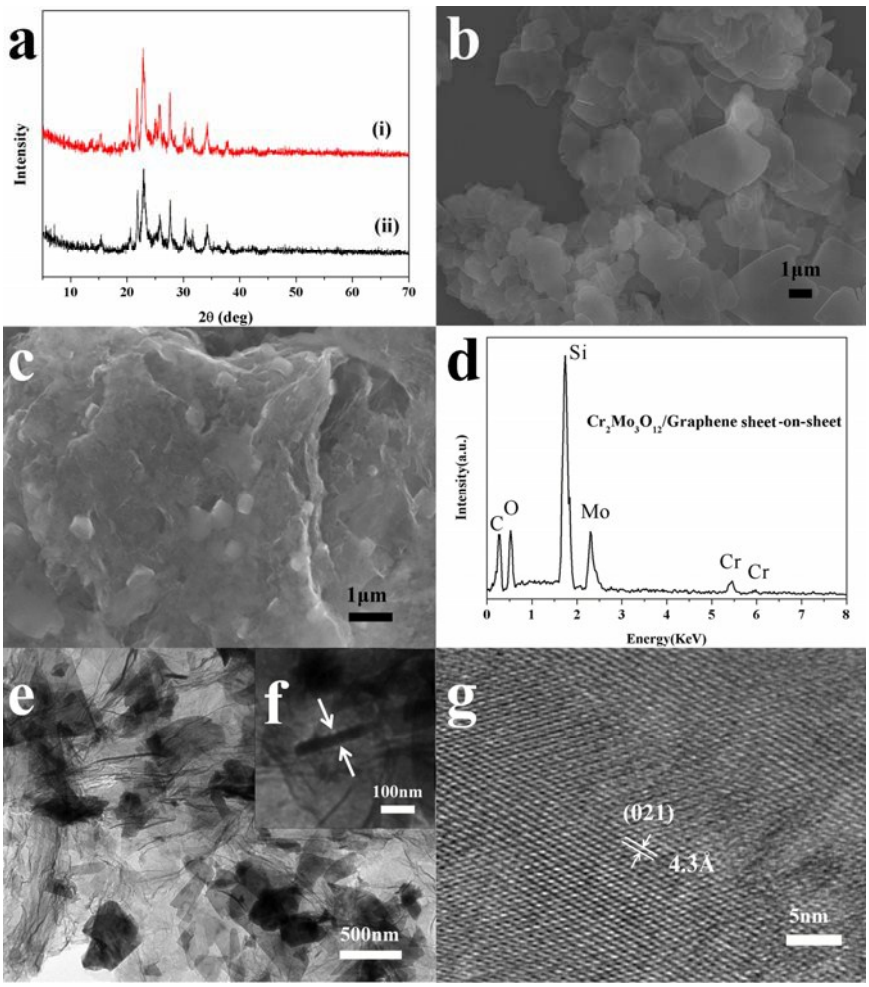

Fig. 6 (a) XRD patterns of (i) the $Cr_2Mo_3O_{12}$/graphene sheet-on-sheet composite and (ii) $Cr_2Mo_3O_{12}$ nanosheets, (b) SEM image of $Cr_2Mo_3O_{12}$ nanosheets, the $Cr_2Mo_3O_{12}$/graphene sheet-on-sheet composite: (c) SEM image, (d) the EDS spectrum, (e) TEM image, (f) the inset image showing the cross-section, and (g) HRTEM image.

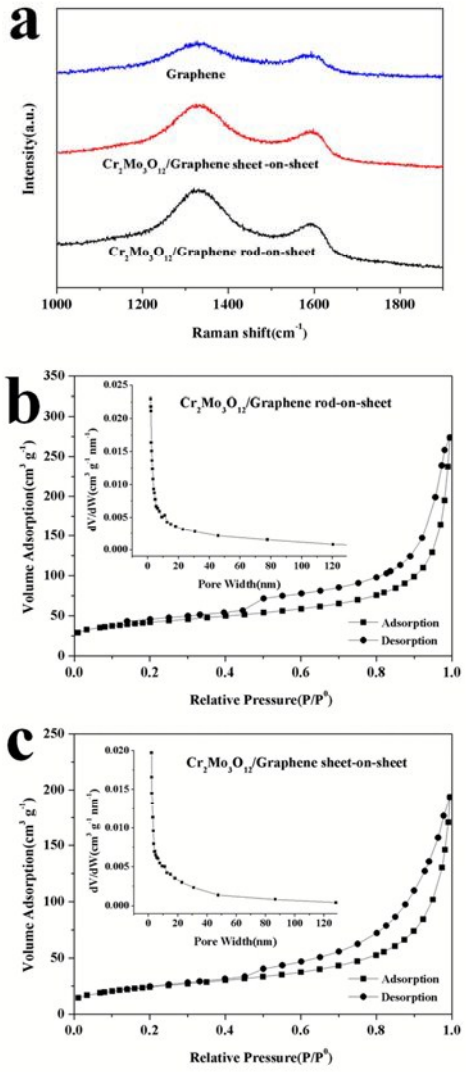

Fig. 7 (a) Raman spectra of various products, Nitrogen adsorption-desorption isotherms: (b) the $Cr_2Mo_3O_{12}$/graphene rod-on-sheet composite, (c) the $Cr_2Mo_3O_{12}$/graphene sheet-on-sheet composite.

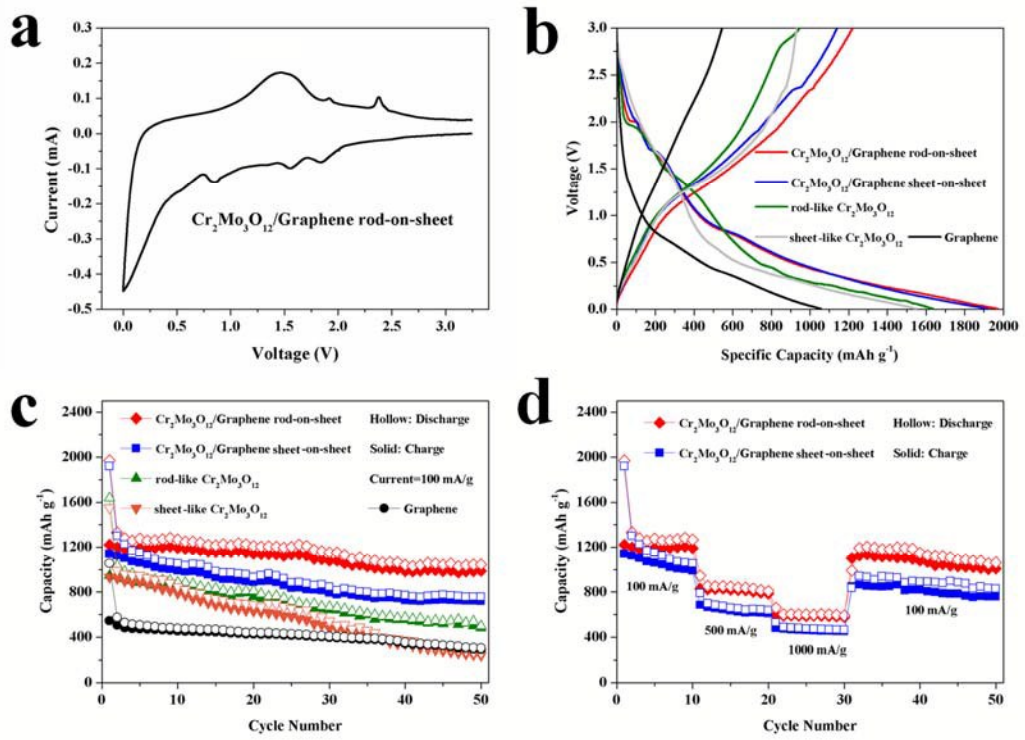

Fig. 8 Electrochemical performances of various $Cr_2Mo_3O_{12}$ based anodes: (a) cyclic voltammograms, (b) the first-cycle discharge (lithium insertion) and charge (lithium extraction) curves, (c) cycling performance at a current density of 100 mA g^{-1} (0.1 C), (d) rate performances at various current densities of 100, 500 and 1000 mA g^{-1}.

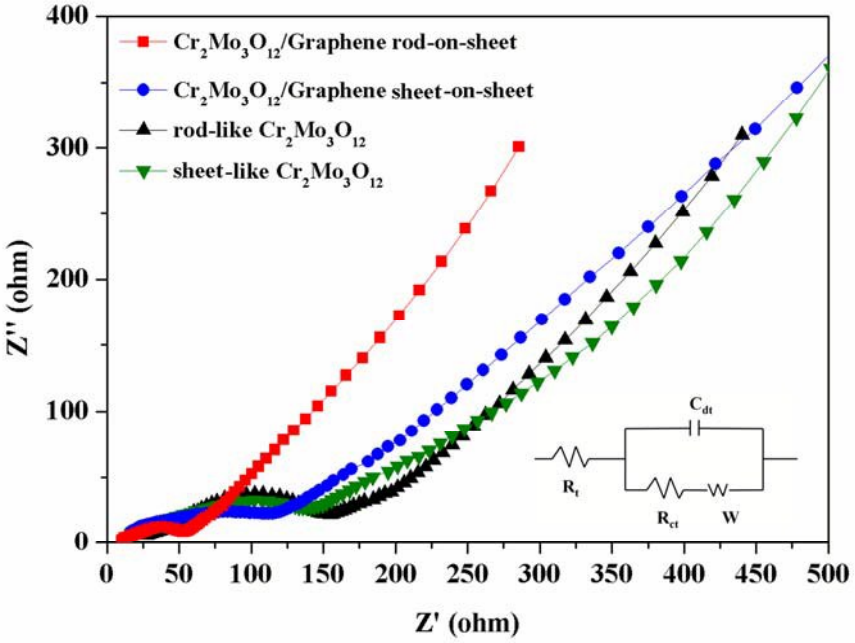

Fig. 9 Nyquist plots of various $Cr_2Mo_3O_{12}$ based anodes.

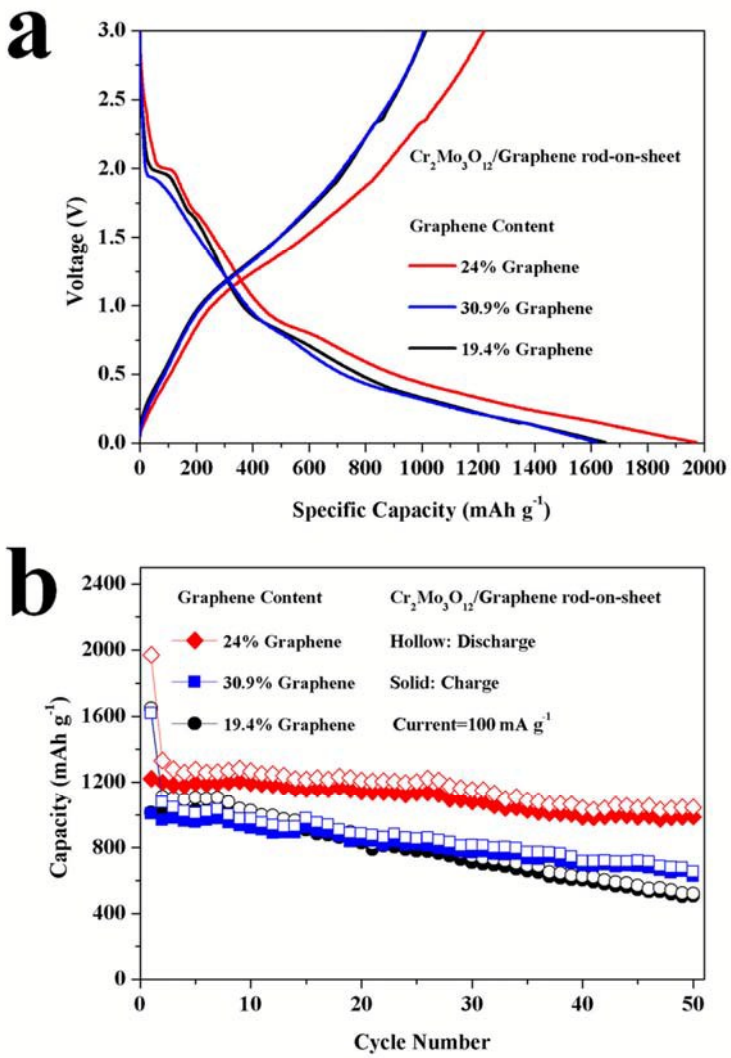

Fig. 10 Electrochemical performances of the $Cr_2Mo_3O_{12}$/graphene rod-on-sheet composites with 19.4 %, 24 % and 30.9 % graphene: (a) the first-cycle discharge (lithium insertion) and charge (lithium extraction) curves, (b) cycling performance at a current density of 100 mA g^{-1} (0.1 C).

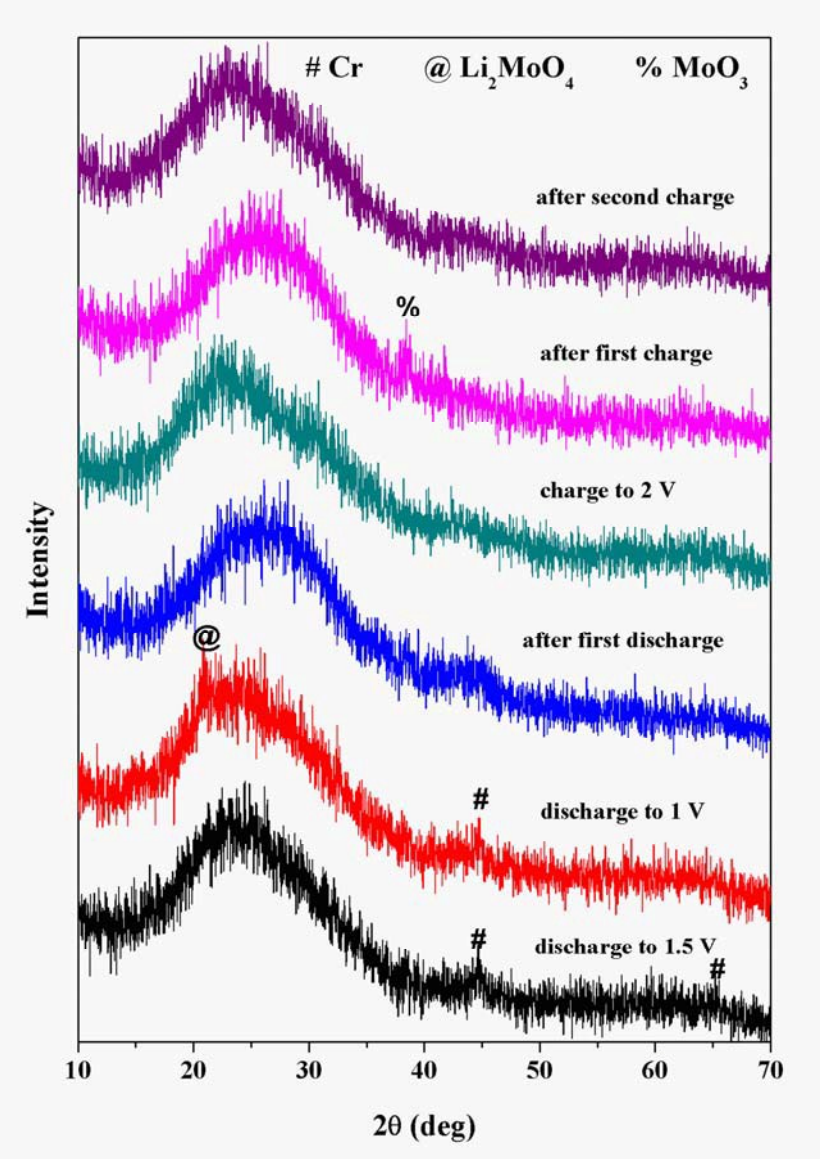

Fig. 11 XRD patterns of the electrodes obtained at different cycling stages.

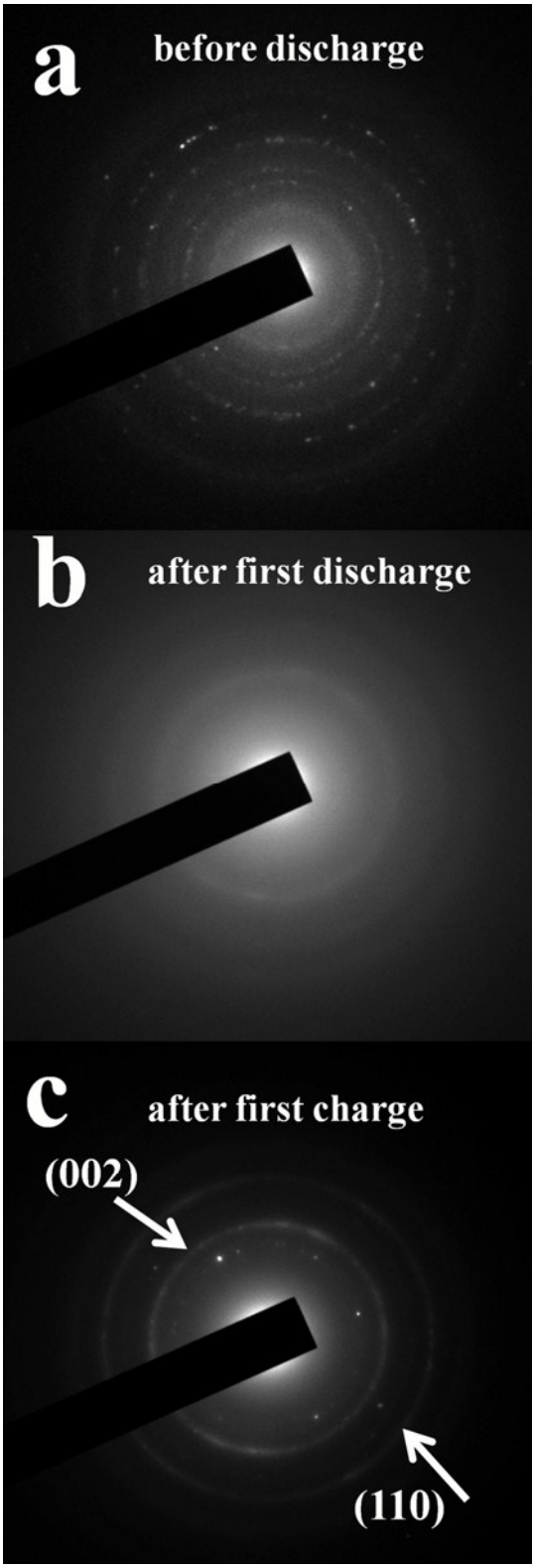

Fig. 12 SAED patterns of the electrodes obtained at different cycling stages: (a) before cycling, (b) after first discharge, and (c) after first charge.

Graphical abstract

New rod-like and sheet-like $Cr_2Mo_3O_{12}$ anodes with and without graphene support are prepared with good Li-storage properties.

New $Cr_2Mo_3O_{12}$-based Anodes：Morphology Tuning and Li-Storage Properties

Lei Guo and Yong Wang*